ACS APPLIED MATERIALS & INTERFACES

Research Article

www.acsami.org

Iron Carbide Nanoparticles Encapsulated in Mesoporous Fe–N-Doped Graphene-Like Carbon Hybrids as Efficient Bifunctional Oxygen Electrocatalysts

Hongliang Jiang, Yifan Yao, Yihua Zhu,* Yanyan Liu, Yunhe Su, Xiaoling Yang, and Chunzhong Li*

Key Laboratory for Ultrafine Materials of Ministry of Education, School of Materials Science and Engineering, East China University of Science and Technology, 130 Meilong Road, Shanghai 200237, China

Supporting Information

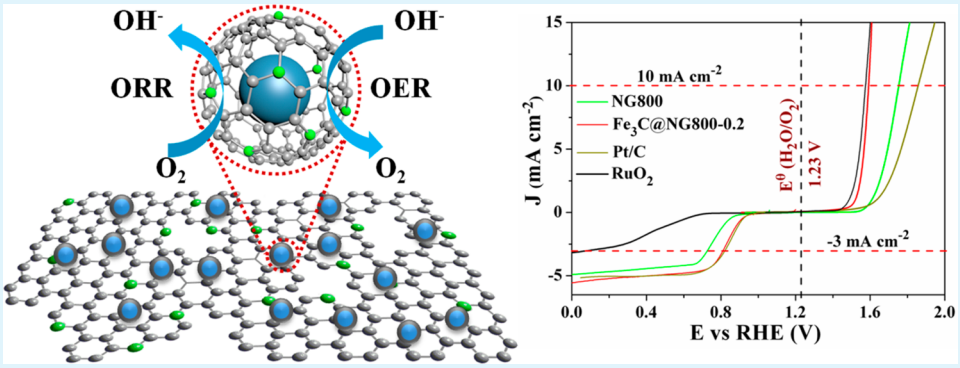

ABSTRACT: It is highly crucial and challenging to develop bifunctional oxygen electrocatalysts for oxygen reduction reactions (ORRs) and oxygen evolution reactions (OERs) in rechargeable metal-air batteries and unitized regenerative fuel cells (URFCs). Herein, a facile and cost-effective strategy is developed to prepare mesoporous Fe–N-doped graphene-like carbon architectures with uniform Fe_3C nanoparticles encapsulated in graphitic layers (Fe_3C@NG) via a one-step solid-state thermal reaction. The optimized Fe_3C@NG800-0.2 catalyst shows comparable ORR activity with the state-of-the-art Pt/C catalyst and OER activity with the benchmarking RuO_2 catalyst. The oxygen electrode activity parameter ΔE (the criteria for judging the overall catalytic activity of bifunctional electrocatalysts) value for Fe_3C@NG800-0.2 is 0.780 V, which surpasses those of Pt/C and RuO_2 catalysts as well as those of most nonprecious metal catalysts. Significantly, excellent long-term catalytic durability holds great promise in fields of rechargeable metal-air batteries and URFCs.

KEYWORDS: *oxygen electrocatalysts, iron carbide, graphitic layers, oxygen reduction reaction, oxygen evolution reaction*

1. INTRODUCTION

With the transition from traditional fossil fuels to clean and sustainable energy, alternative energy storage and conversion devices have gained global attention. One of the most available pathways for energy usage is the electrochemical consumption and generation of fuels,[1] which is not limited by the Carnot cycle. Rechargeable metal-air batteries[2,3] and unitized regenerative fuel cells (URFCs)[4−7] are the two typical energy conversions via electrochemical reactions. In URFCs, through electrochemical water splitting, energy can be stored in H_2 and O_2, and then the energy can be released by their subsequent recombination. Similarly, in rechargeable metal-air batteries, the energy carrier is metals, such as lithium (or Zn, Mg, Al, etc.). In this case, instead the formation and reduction of water, the energy storage and conversion processes can be achieved by the formation and reduction of metal oxide.[8,9] The heart of these technologies is the oxygen reduction reaction and the oxygen evolution reaction (ORR and OER).[10−13] However, the sluggish oxygen electrode kinetics blocks their development and commercialization, which contributes a 15% power loss.[14] To address this issue, the development of highly efficient and cost-effective catalysts for ORR and OER are key priorities.[15−18] Presently, Pt-based materials have been regarded as state-of-the-art catalysts for ORR;[19] the greatest OER catalysts consist of FeNi, Ru, and Ir oxides.[20,21] Nevertheless, Ru and Ir oxides are poor for the ORR;[22] Pt exhibits inferior activity for the OER.[20,23,24] These catalysts have only single excellent catalytic activity, which are not favorable as bifunctional oxygen electrocatalysts in rechargeable metal-air batteries and URFCs. In addition, the prohibitive cost and poor stability are hampering their further large-scale applications. Therefore, extensive efforts have been devoted to nonprecious metal bifunctional catalysts for reversible oxygen catalysis with high activity, low-cost, and superior stability.[25−27]

Received: July 25, 2015
Accepted: September 15, 2015
Published: September 15, 2015

DOI: 10.1021/acsami.5b06708
ACS Appl. Mater. Interfaces 2015, 7, 21511−21520

Recently, one type of alternative to precious metal catalysts for both ORR and OER, transition-metal and nitrogen-doped carbon materials (M-N/C with M = Fe, Co, Ni, etc.) have attracted tremendous interest.[28−31] Among these M-N/C, Fe- or Fe_3C-based materials has shown outstanding advantages due to prominent electrocatalytic performance. Xing and co-workers reported that the Fe_3C encapsulated in hierarchically porous nitrogen-doped carbon materials exhibited excellent activity and stability toward the ORR in both alkaline and acidic media.[32] The Chen research group reported an advanced multifunctonal electrocatalyst with appealing ORR and OER activity in which Fe nanoparticles were encapsulated in the inside of carbon nanotubes.[33] As reported by Bao and co-workers in a series of studies,[34,35] the encapsulated metal NPs can tune redox properties of the surrounding carbon layer owing to a unique host−guest electronic interaction,[35] leading to the formation of catalytic functionalities. Meanwhile, the catalytic activity can be further improved by nitrogen-doping, which is attributable to the formation of nitrogen-containing active sites ($C-N_x$ and $Fe-N_x$). One sample is nitrogen-doped hollow carbon spheres with Fe_3C encased in graphitic layers,[36] which showed apparently higher ORR activity compared to that of the control sample without Fe_3C or nitrogen doping. Conversely, from the angle of subject−object texture relationship, how the metal phase distributes on te carbon matrix significantly affects the catalytic activity. Graphene or graphene-like two-dimensional nanosheet materials are excellent electrode materials for electrochemical reactions due to their high mechanical strength, large surface area, and excellent electrical conductivity.[37−39] As a result, porous structures with transition metal loading on the two-dimensional materials enlarge the density of the active sites and facilitate mass transport. From the above-mentioned discussion, it still remains a great challenge to develop a facile and scalable strategy for producing the Fe- or Fe_3C-based efficient bifunctional oxygen electrocatalysts with a two-dimensional layered structure.

In this study, we present a facile approach for the fabrication of porous Fe−N-doped graphene-like carbon hybrids with Fe_3C encapsulated in graphitic layers (Fe_3C@NG) via a one-step solid-state thermal reaction. Moreover, these precursors (glucose, urea, and $Fe(NO_3)_3{\cdot}6H_2O$) are suitable for large-scale fabrication due to being environmentally friendly and easily obtained. These resulting Fe_3C nanoparticles encapsulated in graphitic layers are well dispersed on the nitrogen-doped graphene-like carbon sheets. The Fe_3C nanoparticles are chemically stable owing to the protection of graphitic layers. The optimized samples showed efficient and robust electrocatalytic performance toward both the ORR and OER under alkaline conditions. The activation effect of Fe_3C on the surrounding graphitic layers and nitrogen-containing active sites ($C-N_x$) probably plays a synergetic role in the remarkable electrocatalytic capability of Fe_3C@NG.

2. EXPERIMENTAL SECTION

2.1. Reagents and Materials. Nafion (5 wt %) and RuO_2 were obtained from Sigma-Aldrich. Pt/C (20 wt %) was obtained from Johnson-Matthey. All other chemicals were purchased from Shanghai Lingfeng Chemical Reagent Co. Ltd., were of analytical grade, and were used as received without further purification. Notably, all cation and anion content of all sensitive impurities (Cl^-, SO_4^{2-}, PO_4^{3-}, Fe, Ni, etc.) in KOH are below 0.005 wt %. Ultrapure water (18 MΩ cm) was used for all experiments.

2.2. Synthesis and Preparation. In a typical procedure, urea (10 g), glucose (0.5 g), the desired amount (0.1, 0.2, and 0.3 g) of iron(III) nitrate hexahydrate ($Fe(NO_3)_3{\cdot}6H_2O$), and ultrapure water (100 mL) were stirred at 80 °C to remove water. The dried Fe_3C@NG precursor was placed into a crucible and then heated to an appointed temperature (700, 800, and 900 °C) with a rate of 3 °C min^{-1} for 2 h in Ar atmosphere. The products were referred to as Fe_3C@NGT-X with T being the annealing temperature and X being the amount of $Fe(NO_3)_3{\cdot}6H_2O$. For comparison, preparation of the N-doped graphene-like carbon materials (denoted as NG800) and Fe_3C-based carbon materials (Fe_3C@C) were the same as Fe_3C@NG800-X, except the raw materials were without the addition of $Fe(NO_3)_3{\cdot}6H_2O$ and urea, respectively. To remove ORR unstable phases, the annealing products were leached in 0.5 M H_2SO_4 solution at 80 °C for 8 h, followed by centrifugation collection and were thoroughly washed with deionized water.

2.3. Instruments. The morphology of the samples was characterized using transmission electron microscopy (JEOL JEM-2100) and scanning electron microscopy (FE-SEM: S-4800). The powder X-ray diffraction (PXRD) data were carried out on a D/Max2550 VB/PC diffractometer (40 kV, 200 mA) using Cu Kα as the radiation. The Fe content was measured by thermogravimetric analysis. The nitrogen adsorption/desorption measurements were used to investigate the specific surface area, pore volume, and pore size of samples. Raman spectra were recorded with a Bruker RFS 100/S spectrometer. X-ray photoelectron spectroscopy (XPS) obtained with VG ESCA 2000 with a magnesium anode was used to demonstrate the content and the doping types of carbon, nitrogen, and Fe. All data were corrected using the C 1s peak at 284.8 eV as an internal standard.

2.4. Electrochemical Measurements. Electrochemical experiments were carried out in a three electrode cell connected to an electrochemical analyzer (CHI 760D). Ag/AgCl with saturated KCl and Pt wire were used as reference and counter electrode, respectively. Four milligrams of as-prepared samples or Pt/C (RuO_2) was ultrasonically dispersed in 1 mL of mixed solvent (3:1 water/2-propanol (v/v)) with 50 μL of Nafion solution. Ten microliters of catalyst suspensions was transferred onto the glassy carbon electrode (RDE, 0.196 cm^2, Pine Research Instrumentation, USA) surface and allowed to dry at room temperature for 30 min (catalyst loading: ~0.20 mg cm^{-2}). According to $E_{RHE} = E_{Ag/AgCl} + 0.989$ V (Figure S1 in the Supporting Information), the potential measured against an Ag/AgCl electrode was converted to the potential versus the reversible hydrogen electrode (RHE). After correction for the capacitive current, all the currents presented in the figures are Faradaic currents. All data were obtained after repetitive cycling between ORR and OER 20 times.

ORR Measurements. The working electrode was cycled at least 10 times before data were recorded at a scan rate of 10 mV s^{-1}. The rotating disk electrode (RDE) and rotating ring-disk electrode (RRDE) voltammograms were recorded in the O_2-saturated 0.1 M KOH solution with a scan rate of 10 mV s^{-1}. In the RRDE system, the potential of the Pt ring electrode was set to 1.50 V (vs RHE). The H_2O_2 yield ($\%H_2O_2$) and electron transfer number (n) were calculated by the followed equations[40,41]

$$\%H_2O_2 = 200 \times \frac{I_R/N}{I_D + I_R/N} \quad (1)$$

$$n = 4 \times \frac{I_D}{I_D + I_R/N} \quad (2)$$

where I_D and I_R are the disk and ring currents, and N is the ring current collection efficiency (37%).

OER Measurements. OER RDE tests were performed in O_2-saturated 0.1 M KOH solution with the potential range from 1.0 to 1.9 V (vs RHE). All data were corrected for the *iR* contribution within the cell, where *R* is the ionic resistance from the solution. To detect H_2O_2 oxidation and O_2 reduction during the OER process, RRDE measurements were also conducted on the Fe_3C@NG800-0.2 catalyst, and the potential of the Pt ring electrode was set to 1.50 and 0.45 V (vs RHE), respectively. For probing O_2 reduction during the OER process, the KOH solution was saturated with N_2. The stability was

DOI: 10.1021/acsami.5b06708
ACS Appl. Mater. Interfaces 2015, 7, 21511−21520

evaluated by chronoamperometry tests at 1.59 V (vs RHE) with a rotation rate of 1600 rpm.

3. RESULTS AND DISCUSSION

As illustrated in Figure 1a, the Fe_3C@NGT-X was prepared by simple annealing treatment of a homogeneous mixture of urea,

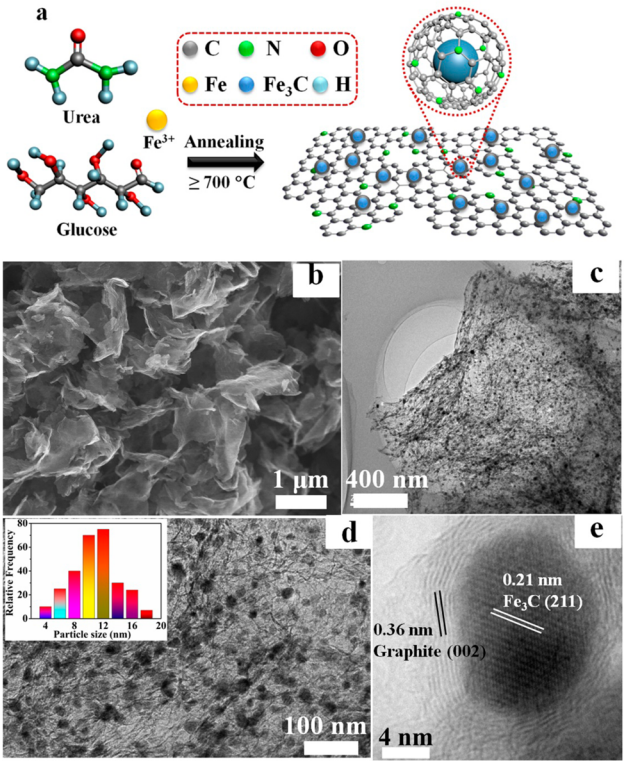

Figure 1. (a) Schematic diagram of the fabrication of Fe_3C@NG. (b) SEM images, (c, d) TEM images, and (e) HRTEM images of Fe_3C@NG800-0.2. The inset of (d) is the corresponding particle size distribution histogram.

glucose, and metal salts ($Fe(NO_3)_3{\cdot}6H_2O$) at a desired temperature (700, 800, and 900 °C) in Ar atmosphere (for details see the Experimental Section). The structure and morphology of the prepared Fe_3C@NG800-0.2 were investigated by SEM and TEM measurements. As revealed in Figure 1b, the resulting hybrids show typical graphene-like sheet morphology in which no obvious nanoparticles can be seen, probably due to the very small size of Fe_3C. TEM images (Figure 1c) show that the formed Fe_3C NPs are uniformly loaded on thin carbon sheets (Figure 1d). The size distribution histogram (inset of Figure 1d) demonstrates that these Fe_3C NPs have an average size of 11.1 nm with a narrow distribution. Figure 1e demonstrates the well-defined crystalline lattice spacing of 0.21 and 0.36 nm, which matches well with the (211) planes of the Fe_3C phase (JCPDS, No. 65-2411) and the (002) planes of the graphite phase, respectively.[32] Notably, these Fe_3C NPs are surrounded by a few graphitic carbon layers despite acid washing, implying good electrochemical activity and stability for catalytic reactions. X-ray diffraction (XRD) patterns were further used to characterize the Fe_3C@NG800-0.2 (Figure S2). The diffraction peak at 26.1° suggests the formation of graphitic carbon during the pyrolysis. The rest of the diffraction peaks are characteristic of the crystalline planes of the Fe_3C phase (JCPDS, No. 65-2411). The non-Fe_3C samples (NG800) without the addition of $Fe(NO_3)_3{\cdot}6H_2O$ also exhibited graphene-like sheet morphology, except for the absence of Fe_3C NPs (Figure S3). The XPS spectrum indicates the absence of any metal in NG800. Compared with Fe- or Fe_3C-based carbon nanotube catalysts recently reported that were achieved by similar methods,[35,36] no carbon nanotubes could be found in Fe_3C@NG800-0.2. It is believed that the formation of layered g-C_3N_4 (Figure S4) from urea plays a key role on such a structure of the graphene-like sheet. Chen and co-workers reported that layered graphitic carbon nitride (g-C_3N_4) could be formed when urea is thermally treated at 600 °C.[42] Similarly, as reported by the Sun research group,[38] crumpled BCN nanosheets have been successfully synthesized by annealing urea, boric acid, and polyethylene glycol (PEG). In our work, the Fe species and carbon intermediates can enter into the interlayer space of layered C_3N_4, which is from the polymerization of urea. Such a confinement effect obviously depressed the growth of carbon nanotubes and favored the simultaneous formation of small units. When the C_3N_4 template undergoes complete thermolysis at >700 °C, the graphene-like sheets are liberated.[43,44] Meanwhile, Fe species were reduced to Fe_3C NPs under inert gas (Ar flow), and then, the resulting Fe_3C@NG hybrids were obtained.

The bulk elemental composition of the Fe_3C@NG800-0.2 hybrids was analyzed by thermogravimetric analysis (TGA) and an energy dispersive X-ray analyzer (EDX). After treatment in O_2 atmosphere during TGA, the Fe_3C@NG800-0.2-derived product was identified as Fe_2O_3 (Figure S5). As shown in Figure 2a, on the basis of the mass of Fe_2O_3 (40.2 wt %) left after 800 °C, the Fe content was estimated to be 29.6 wt % in the original Fe_3C@NG800-0.2 hybrids. Moreover, the EDS result (Figure 2b) shows that the C peak at 0.20 keV accompanies an N tail peak and three Fe peaks at approximately 0.71, 6.39, and 7.05 keV, corresponding with $FeL_{\alpha 1}$, $FeL_{\beta 1}$, and $FeL_{\gamma 1}$, respectively. As-synthesized Fe_3C@NG800-0.2 was comprised of 29.4 wt % Fe, 56.3 wt % C, 9.7 wt % O, and 4.6 wt % N, which is in good agreement with the TGA result. Raman measurements were conducted to demonstrate the structure defects. As shown in Figure 2c, the D- and G-bands at approximately 1357 and 1577 cm^{-1} clearly demonstrate the existence of disorder and graphitic carbon.[45,46] In addition, the intensity ratio of the D- and G-bands (I_D/I_G) slightly decreased with increasing annealing temperature at 1.06 for Fe_3C@NG700-0.2, 1.01 for Fe_3C@NG800-0.2, and 0.99 for Fe_3C@NG900-0.2, indicating that the graphitization can be enhanced at higher temperature.[47] The specific surface area and pore size of the hybrids were investigated by measuring the N_2 adsorption/desorption isotherm. Figure 2d shows that Fe_3C@NG900-0.2 has a specific surface area of ~755.6 $m^2\ g^{-1}$ and that the mesoporous structure entered at 3.85 nm, which is demonstrated by the pore size distributions (the inset of Figure 2d). Notably, the annealing temperature highly influenced the surface area of the hybrids. The other two samples have BET surface areas of 576.4 (Fe_3C@NG900-0.2) and 401.2 $m^2\ g^{-1}$ (Fe_3C@NG700-0.2) (Figure S6). Similar porous structures of the three samples are probably attributed to a large amount of gas from decomposition of the carbon nitride.[43,44] That is, 800 °C is the optimized temperature at which the maximum surface area is obtained.

For the doped element and bonding configurations to be further elucidated, XPS measurements were conducted on Fe_3C@NGT-0.2. As revealed, the survey spectrum of Fe_3C@NG800-0.2 demonstrates the presence of C (89.53 at%), N

DOI: 10.1021/acsami.5b06708
ACS Appl. Mater. Interfaces 2015, 7, 21511−21520

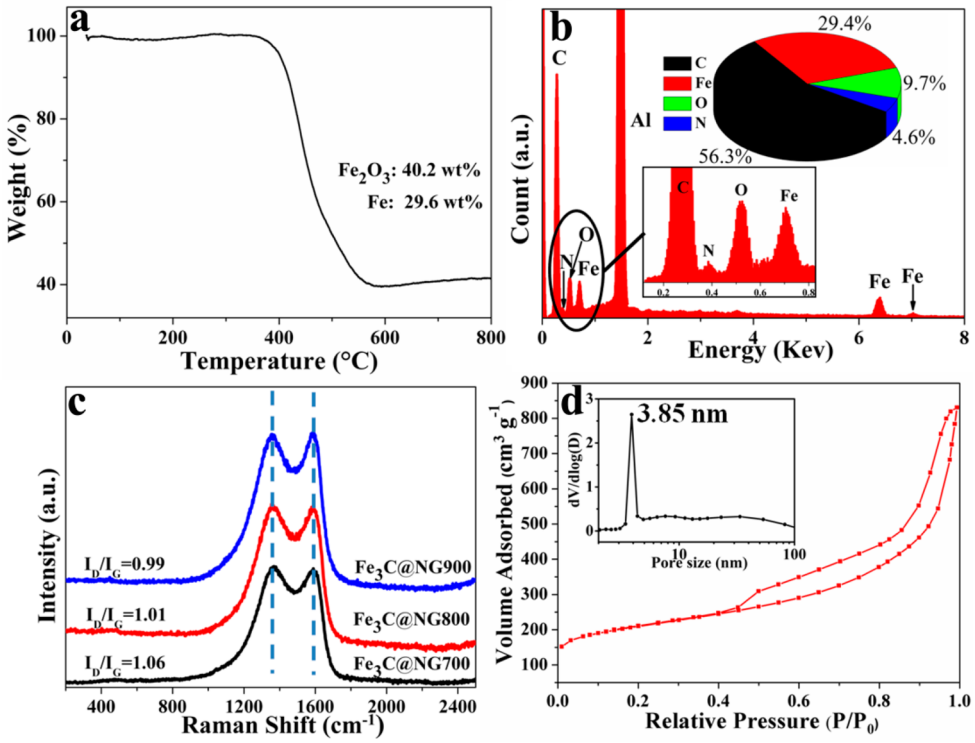

Figure 2. (a) TGA curve of Fe_3C@NG800-0.2 measured from 25 to 800 °C in atmospheric air with a heating rate of 10 °C min^{-1}. (b) Energy-dispersive X-ray spectroscopy (EDS) of Fe_3C@NG800-0.2. Aluminum foil was used as the substrate material. The acceleration voltage was 15 eV. (c) Raman spectra of Fe_3C@NG800-0.2. (d) N_2 adsorption/desorption isotherm of Fe_3C@NG800-0.2 and the corresponding pore size distribution (inset).

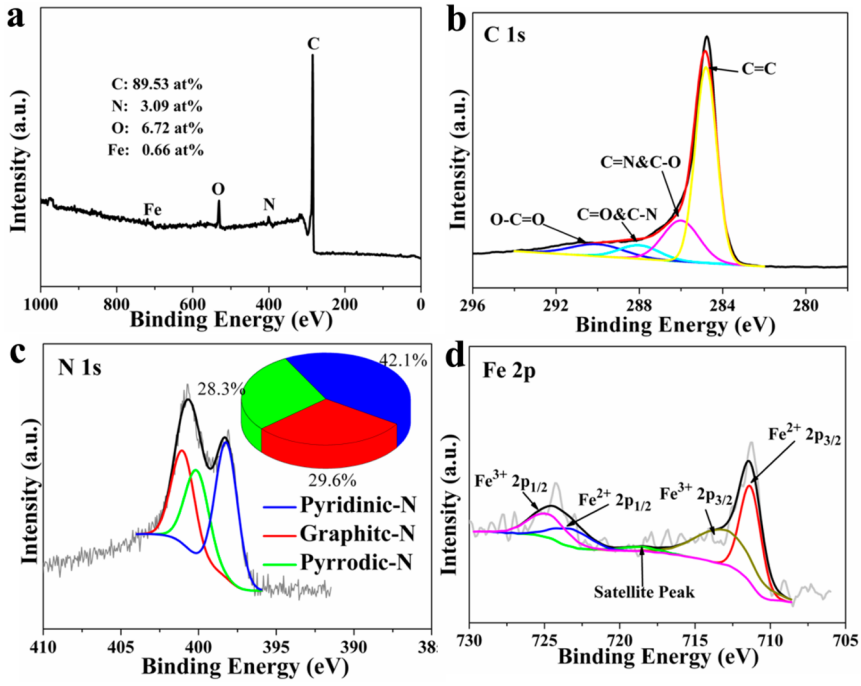

Figure 3. (a) Wide XPS survey of the Fe_3C@NG800-0.2. High resolution (b) C 1s, (c) N 1s, and (d) Fe 2p spectra of the Fe_3C@NG800-0.2.

(3.09 at%), O (6.72 at%), and Fe (0.66 at%) elements without any other element (Figure 3a). The content of Fe obtained from XPS is much lower than that calculated from the TGA, which is because XPS analysis can hardly measure the Fe_3C NPs incorporated in carbon layers due to its detecting depth (~5 nm).[48,49] The C 1s peaks were centered at 284.8 eV along with a tail at higher binding energies.[50,51] Furthermore, the high-resolution spectrum of C 1s (Figure 3b) can be deconvoluted to several single peaks corresponding to O−C═O, C−N and C═O, C═N and C−O, and C═C, indicating the existence of heteroatoms in hybrids.[52] As shown in Figure 3c, the N 1s spectra can be deconvoluted to

DOI: 10.1021/acsami.5b06708
ACS Appl. Mater. Interfaces 2015, 7, 21511−21520

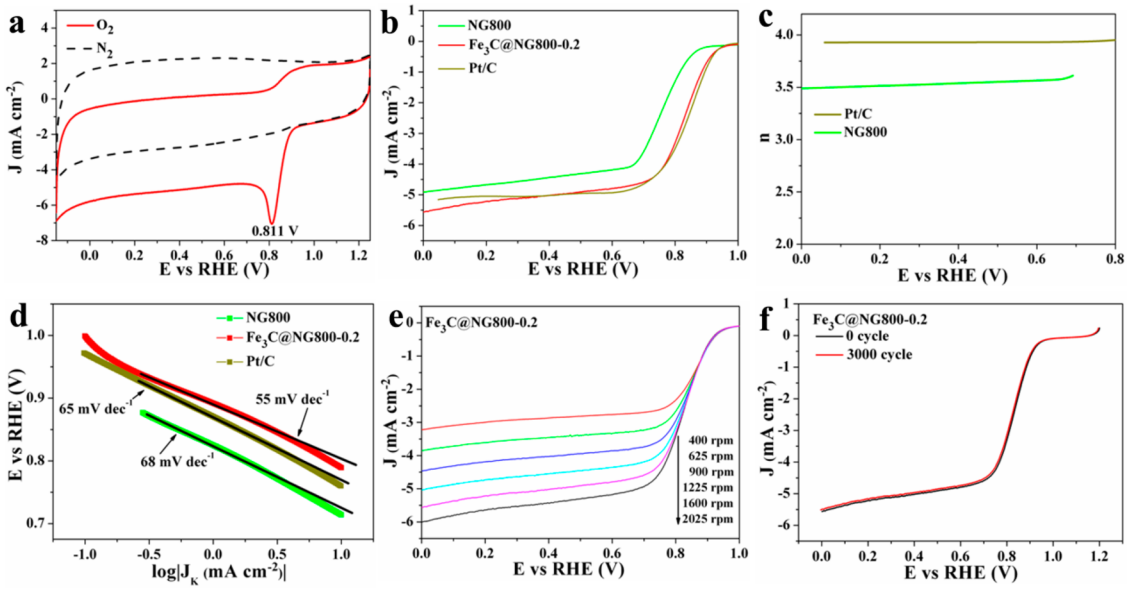

Figure 4. (a) CVs of Fe_3C@NG800-0.2 with a scan rate of 50 mV s^{-1}. (b) RDE LSV curves of Fe_3C@NG800-0.2, NG800, and Pt/C at a rotation rate of 1600 rpm with a scan rate of 10 mV s^{-1}. (c) The number of electron transfer (n) of NG800 and Pt/C catalyst at a rotation speed of 1600 rpm. (d) Tafel plots of the Fe_3C@NG800-0.2, NG800, and Pt/C catalysts. (e) LSV curves of the Fe_3C@NG800-0.2 catalyst with different rotation rates. (f) LSV curves of the Fe_3C@NG800-0.2 catalyst for ORR in O_2-saturated 0.10 M KOH before and after 3000 cycles.

three peaks at 398.3, 400.1, and 401.2 eV, which are consistent with pyridinic-N, pyrrolic-N, and graphitic-N (Figure S7), respectively, suggesting that nitrogen was successfully doped into the carbon framework.[53] In addition, the concentrations of the different nitrogen dopants were quantified based on the integrated peak areas (inset of Figure 3c), and it can be concluded that pyridinic-N and graphitic-N were the dominant species, which are generally considered as efficient ORR active sites.[53,54] The content of N decreases upon increasing the annealing temperature, which is attributed to instability of N dopant elevated temperature (Table S1). Furthermore, Figure 3d shows the high-resolution spectra of Fe 2p, which can be deconvoluted to two pairs of peaks for Fe^{3+} (713.1 and 725.0 eV) and Fe^{2+} (711.4 and 723.1 eV) with a satellite peak at 717.8 eV.[53] Notably, the signal of Fe^0 at 707 eV is not observed, further demonstrating that Fe_3C NPs are encapsulated by carbon layers. According to a previous report, the peak at 711.4 eV in the Fe $2p_{3/2}$ XPS spectrum demonstrates the existence of Fe−N_x bonding.[55]

The annealing temperature highly influences the electrocatalytic activities of these M-N/C, which is demonstrated by a large number of studies.[56,57] Therefore, both the ORR and OER activity of the Fe_3C@NGT-0.2 catalysts prepared at different temperature are first researched through RRDE and RDE measurements performed in O_2-saturated 0.1 M KOH solutions, respectively. Linear sweep voltammetry (LSV) curves indicate that the Fe_3C@NG800-0.2 catalyst has the most positive onset potential (+ 0.98 V) and largest diffusion-limited current density among the three Fe_3C@NGT-0.2 catalysts (Figure S8). The H_2O_2 yield and electron transfer number (n) directly demonstrated excellent ORR activity of the Fe_3C@NG800-0.2 catalyst. As shown in Figure S8b, for the Fe_3C@NG800-0.2 catalyst, the H_2O_2 yield was below 5% at all potentials, which is lowest among the other two catalysts. Accordingly, the average electron transfer number (n) was 3.94, which is obviously highest among the Fe_3C@NGT-0.2 catalysts (Figure S8c). In addition, the Fe_3C@NG800-0.2 catalyst also shows the best OER activity in terms of overpotentials (η), obtaining a current density of 10 mA cm^{-2}. These results are probably attributable to a balance of porosity, electrical conductivity, and type and density of active sites at the optimized temperature (800 °C).[30,58] The Fe_3C@NG700-0.2 sample prepared at low temperature has low electrical conductivity, which blocks the charge transfer. The Fe_3C@NG900-0.2 sample prepared at high temperature is a lack of catalytically active sites. In addition, the Fe_3C@NG800-0.2, which has the largest specific surface area, is favorable for active site exposure and rapid ORR (or OER) relevant species transport. Therefore, the Fe_3C@NG800-0.2 catalyst shows optimized ORR and OER activity.

The ORR performance of Fe_3C@NG800-0.2 was further evaluated by conducting other electrochemical measurements and compared to other catalysts (NG800 and Pt/C). The cyclic voltammetry (CV) measurements were first performed on the Fe_3C@NG800-0.2 catalyst. As shown in Figure 4a, a well-defined cathodic peak centered at +0.811 V appears when the electrolyte solution is saturated with O_2, suggesting an outstanding ORR catalytic activity for Fe_3C@NG800-0.2 in alkaline media. As shown in Figure 4b, the LSV curves indicate that Fe_3C@NG800-0.2 catalyst has comparable ORR activities with Pt/C catalyst, as revealed by comparable onset potential and diffusion-limited current density in which the onset potential was identified as +0.99 V for Pt/C. Therein, the NG800 catalyst exhibited obviously worse electrocatalytic activity than Fe_3C@NG800-0.2 and Pt/C, indicating that the existence of Fe-related species (Fe_3C or Fe−N_x) significantly enhanced the ORR activities. In addition, the H_2O_2 yield (Figure S9) and corresponding electron transfer number (n) (Figure 4c) of NG800 and Pt/C catalysts further indicate that the Fe_3C@NG800-0.2 catalyst has a similar four-electron ORR process as that of the Pt/C catalyst. Tafel slope of the Fe_3C@NG800-0.2 catalyst also indicates a similar reaction mechanism with the Pt/C catalyst (Figure 4d). LSV curves of the Fe_3C@NG800-0.2 catalyst were also recorded through the rotating

DOI: 10.1021/acsami.5b06708
ACS Appl. Mater. Interfaces 2015, 7, 21511−21520

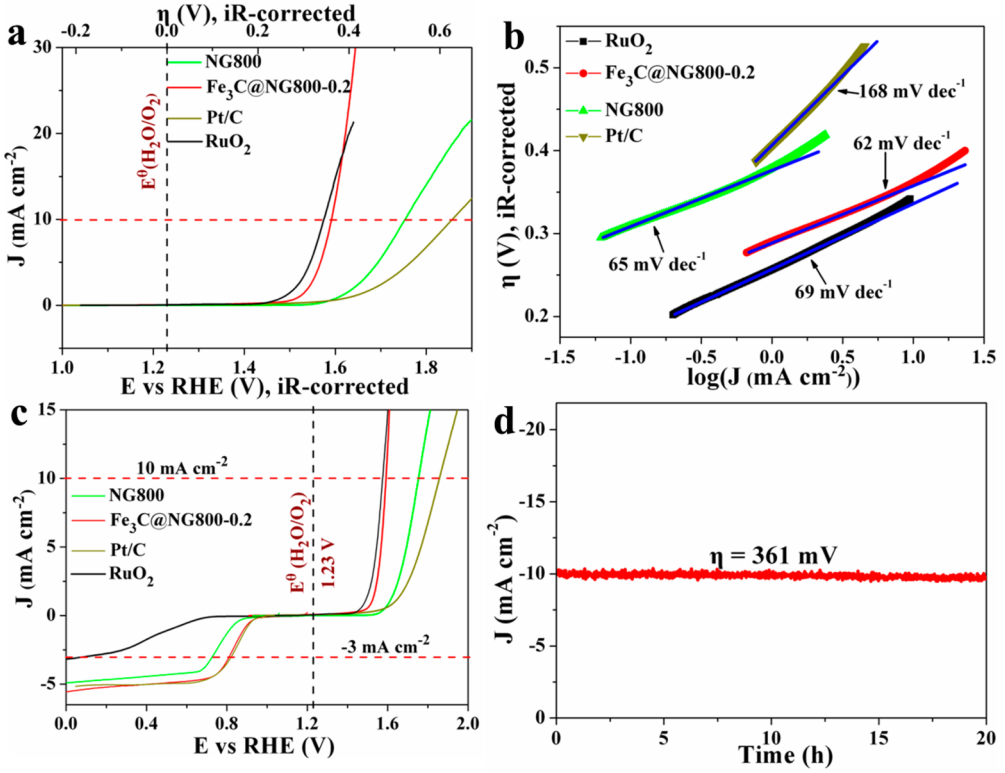

Figure 5. (a) Polarization curves of all catalysts. The ionic resistance (~45 Ω) from the solution was determined via an *iR* compensation test. (b) Tafel plots of all catalysts from the polarization curves. (c) Oxygen electrode activities within the ORR and OER potential window of various catalysts dispersed on the glass carbon electrode in O_2-saturated 0.1 M KOH. (d) Time dependence of cathodic current density for Fe_3C@NG800-0.2 over 20 h at fixed overpotentials of 361 mV.

disk electrode (RDE) measurements at different rotating speeds from 400 to 2025 rpm (Figure 4e). Typically, the limiting current density of the three sample electrodes increased with increasing rotation speed (from 400 to 2025 rpm), which is in accordance with other studies.[59,60] The stability of the Fe_3C@NG800-0.2 catalyst was also evaluated by LSV measurements in O_2-saturated 0.10 M KOH before and after 3000 cycles. The ORR polarization curve shows almost no change after 3000 cycles (Figure 4f). In contrast, the half-wave potentials and limiting current density of thePt/C catalyst show obvious diminishment (Figure S11). These results clearly indicate that the catalytically active sites on the Fe_3C@NG800-0.2 catalyst are much more stable than those on the commercial Pt/C electrode.

The OER activities of Fe_3C@NGT-X and other catalysts were evaluated by linear sweep voltammograms (LSVs) with potentials from 1.0 to 1.9 V (see Experimental Section for details). As revealed by the polarization curves plotted in Figure 5a, Fe_3C@NG800-0.2 exhibits much earlier onset potential and greater current density than that of Pt/C or NG800, which is comparable to that of the state-of-the-art RuO_2 catalyst (Sigma-Aldrich). Moreover, comparing the overpotential (η) of achieving a current density of 10 mA cm^{-2} is very meaningful, which is a metric relevant to compare the OER activities.[61] In our case, Fe_3C@NG800-0.2 can obtain such a current density at a small η of ~0.361 V, approaching the η requirement for the RuO_2 catalyst, and it is much smaller than that of non-Fe_3C NG800 and commercial Pt/C catalyst. The OER kinetics of the above catalysts are further probed by the Tafel slope. As shown in Figure 5b, the resulting Tafel slopes are approximately 62, 69, 65, and 168 mV dec^{-1} for Fe_3C@NG800-0.2, commercial RuO_2, NG800, and commercial Pt/C, respectively. Notably, the Fe_3C@NG800-0.2 exhibits the smallest Tafel slope and is therefore the most efficient OER catalyst among all the catalysts in this study, suggesting superior intrinsic OER kinetics of this kind of Fe_3C-based material even compared with that of the RuO_2 catalyst. Meanwhile, the better catalytic activity of Fe_3C@NG800-0.2 compared to the NG800 catalyst demonstrated that the Fe-related species plays an important role on excellent OER activity, which is further elaborated in the following discussion. To better compare the bifunctional catalytic activities, it is a common method to calculate the oxygen electrode activity parameter ΔE ($\Delta E = E_{J10,OER} - E_{J\text{-}3,ORR}$). Obviously, the Fe_3C@NG800-0.2 exhibited the smallest ΔE (0.78 V) (Table S2), implying best bifunctional catalytic activity and the most potential for practical applications. In addition, compared to some reported bifunctional electrocatalysts (Table S3), Fe_3C@NG800-0.2 also remains competitive, showing great promise for use in URFCs and rechargeable metal-air batteries. To further probe intermediates and gain insight into the reaction mechanism of OER, RRDE measurements were also conducted on the Fe_3C@NG800-0.2 catalyst with sweeping potentials from 1.0 to 1.8 V (Figure S12). When the Pt ring potential was set to 1.50 V, no obvious ring current was observed, thus implying negligible formation of H_2O_2. Interestingly, when the RRDE measurement was performed on N_2-saturated 0.1 M KOH solution with a Pt ring potential of 0.45 V, an obvious ring current appeared from around 1.5 V, which is close to the onset potential of the Fe_3C@NG800-0.2 catalyst in the OER process. In addition, the ring current increases relevantly with the increasing disk current. In N_2-saturated 0.1 M KOH solution, the ring current with a Pt ring potential of 0.45 V was

DOI: 10.1021/acsami.5b06708
ACS Appl. Mater. Interfaces 2015, 7, 21511−21520

attributed to the reduction of O_2, further suggesting that disk oxidation current is related to the OER. The two RRDE measurements described above and related results demonstrated that water oxidation on the Fe_3C@NG800-0.2 catalyst proceeded through a four-electron route with O_2 evolution, which is also similar to some previous studies on the oxygen evolution reaction on carbon-based materials.[33,62,63] Furthermore, the catalytic durability of Fe_3C@NG800-0.2 toward OER is also evaluated by the time dependence of the current density at fixed overpotentials of 361 mV (Figure 5d). The negligible loss of current density after 20 h demonstrates the superior durability of the Fe_3C@NG800-0.2 catalyst.

To further explore the influence of Fe-related species (Fe_3C or Fe−N_x) on the electrocatalytic activity, we prepared Fe_3C@NG800-X with various Fe content. RDE measurements of these hybrids suggested that the Fe_3C@NG800-0.2 catalyst was optimized, as revealed by the most positive onset potential and largest current density at the same overpotential (Figure S13). For the Fe_3C@NG800-0.1 catalyst, insufficient $Fe(NO_3)_3\cdot 6H_2O$ precursor meant the formation of fewer Fe-related active sites (Fe_3C or Fe−N_x), which probably leads to worse ORR activity compared to that of the Fe_3C@NG800-0.2 catalyst. When increasing the quantity of $Fe(NO_3)_3\cdot 6H_2O$, the catalytic activity of Fe_3C@NG800-0.3 catalyst is also inferior to that of the Fe_3C@NG800-0.2 catalyst (Figure S13). The performance degradation when overloading Fe_3C may contribute to the much larger Fe_3C nanoparticles (up to ∼100 nm, Figure S14) on nanosheets that can block the pores, which is demonstrated by the obviously smallest BET surface area of Fe_3C@NG800-0.3 (354.5 $m^2\ g^{-1}$, Figure S15).

It is a consensus that pyridinic-N and graphitic-N dopants are active for both ORR and OER.[64,65] A typical work, reported by Xia and co-workers, elaborately studied the ORR and OER catalytic mechanism of N-doped carbon materials.[66] Density functional theory (DFT) calculations indicated that overpotentials of both ORR and OER can be obviously decreased on pyridinic-N- and graphitic-N-doped structures, and the lower overpotential means better catalytic activities. For ORR, electron transfer from adjacent C to N dopants will occur due to stronger electronegativity of N such that the strong electrostatic force between C and O facilitates O_2 adsorption and dissociation on adjacent C atoms.[67] Similarly for OER, the positive carbon atoms also can facilitate adsorption of OH^- ions and promote electron transfer to intermediates (O*, OH*, and OOH*).[62] Conversely, it is of interest that both the ORR and OER catalytic activities of N-doped carbon can be markedly improved by the introduction of a transition metal (Fe, Co, Ni, etc.),[53] the inherent reason for which is highly controversial in current studies. Herein, the role of transition metals on ORR is discussed first. Some researchers proposed that metal−N coordination (mainly Fe−N_x) is catalytically active for ORR.[30] Contrarily, some researchers claimed that the transition metals only serve as catalysts for the formation of active sites, as originally proposed by Wiesener.[67] Despite the inherent contribution of transition metals to ORR, extensive experimental studies have demonstrated that a trace amount of transition metal residues can effectively improve ORR activities of N-doped carbon catalysts.[30,53] Notably, for Fe_3C-based ORR catalysts, the outstanding ORR performance is attributable to other reasons in addition to the factors of the N dopants and Fe−N_x species described above. Bao and co-workers indicated that iron carbide (Fe_xC_y) can tune the redox properties of the surrounding carbon layer via the effect of confinement.[35] In subsequent studies reported by Xing et al., the role of the Fe_3C phase was further revealed by systematic experimental studies.[32,36] Excitingly, through ex situ spectroscopic methods (Mössbauer spectroscopy and synchrotron XAS), Strickland et al. demonstrated that Fe/Fe_xC could assist the stabilization of the peroxide intermediate on the surrounding N-doped carbon layers and promote a $4e^-$ ORR process,[68] which is similar to Bao's study on iron encapsulated within podlike carbon nanotubes.[34] On the basis of the above discussion and compositional characterizations of the Fe_3C@NG800-0.2 catalyst, its superior ORR performance is attributable to a large specific surface area (755.6 $m^2\ g^{-1}$), high percentage of pyridinic-N (42.1%) and graphitic-N (29.6%) dopants, a trace amount of Fe−N_x species, and the existence of an Fe_3C phase. Unlike the ORR, for intrinsic OER active sites of Fe−N/C_x-based electrocatalysts, none of these recent studies can give an accurate and quantitative explanation of how Fe-related species affect OER performance. To further explore how coexistence of Fe-related species (Fe_3C and Fe−N_x) and N dopants influenced the OER catalytic activity, we also prepared Fe_3C-based carbon materials (Fe_3C@C) by the same method as that of Fe_3C@NG800-X except using the raw materials without the addition of urea. The Fe_3C@C shows the interconnected nanoparticle morphology (Figure S16a), further indicating the role of urea on the formation of graphene-like sheets of Fe_3C@NG800-X and NG800. For OER, the Fe_3C@C catalyst shows better catalytic activity than Pt/C in terms of overpotential (η), achieving a current density of 10 mA cm^{-2}, which is slightly worse than NG800 (Figure S16b). The better OER activity of the Fe_3C@NG800-0.2 catalyst than that of Fe_3C@C and NG800 catalysts indicates that the Fe-related species has a positive effect on the OER process of N-doped materials. Nevertheless, a question is which Fe-related component actually enhances the OER catalytic activity: Fe_3C or Fe−N_x. Hashimoto et al.[69] prepared efficient bifunctional Fe/C/N electrocatalysts for bifunctional oxygen electrocatalysts, implying that Fe−N_x and C−N_x are probably active site. Lan et al. has also prepared N-doped Fe/Fe_3C-based excellent bifunctional electrocatalysts from MOFs.[70] These experimental studies suggested that Fe-related species (Fe_3C and Fe−N_x) and N dopants simultaneously enhance the ORR and OER catalytic activity. However, what roles the Fe-related species play needs to be further elaborated, which is under progress.

4. CONCLUSIONS

In summary, a facile and cost-effective strategy is developed to prepare iron carbide nanoparticles encapsulated in mesoporous Fe−N-doped graphene-like carbon hybrids via one-step solid-state reaction of glucose, urea, and $Fe(NO_3)_3\cdot 6H_2O$. The optimized Fe_3C@NG800-0.2 catalyst exhibited excellent bifunctional catalytic activity toward both ORR and OER with high catalytic efficiency and long-term durability, which is even comparable with the state-of-the-art Pt/C and RuO_2 catalyst. More importantly, our presented strategy could be extended to prepare other heteroatom-doped composites for various applications, such as supercapacitors, lithium-ion batteries, and solar cells.

■ ASSOCIATED CONTENT

Supporting Information

Additional texts, figures, and tables as mentioned in the main test. The Supporting Information is available free of charge on

DOI: 10.1021/acsami.5b06708
ACS Appl. Mater. Interfaces 2015, 7, 21511−21520

the ACS Publications website at DOI: 10.1021/acsami.5b06708.

RHE calibration, XRD patterns, TEM and SEM images, XPS spectra, N_2 adsorption/desorption isotherms, nitrogen-doping schematic, XPS atomic percents, RRDE and linear sweep voltammograms, H_2O_2 yields, bifunctional oxygen electrode activity data, and ORR and OER activity comparisons (PDF)

AUTHOR INFORMATION

Corresponding Authors

*E-mail: yhzhu@ecust.edu.cn.

*Tel.: +86-21-64252022. Fax: +86-21-64250624. E-mail: czli@ecust.edu.cn.

Notes

The authors declare no competing financial interest.

ACKNOWLEDGMENTS

This work was supported financially by the National Natural Science Foundation of China (21176083, 21471056, 21236003, and 21206042), the Basic Research Program of Shanghai (13NM1400700, 13NM1400701), and the Fundamental Research Funds for the Central Universities.

REFERENCES

(1) Larcher, D.; Tarascon, J. M. Towards Greener and More Sustainable Batteries for Electrical Energy Storage. *Nat. Chem.* **2015**, *7*, 19−29.

(2) Zhang, J.; Li, P.; Wang, Z.; Qiao, J.; Rooney, D.; Sun, W.; Sun, K. Three-Dimensional Graphene-Co_3O_4 Cathodes for Rechargeable Li-O_2 Batteries. *J. Mater. Chem. A* **2015**, *3*, 1504−1510.

(3) Chen, Z.; Yu, A.; Ahmed, R.; Wang, H.; Li, H.; Chen, Z. Manganese Dioxide Nanotube and Nitrogen-doped Carbon Nanotube Based Composite Bifunctional Catalyst for Rechargeable Zinc-air Battery. *Electrochim. Acta* **2012**, *69*, 295−300.

(4) Guarnieri, M.; Alotto, P.; Moro, F. Modeling the Performance of Hydrogen-Oxygen Unitized Regenerative Proton Exchange Membrane Fuel Cells for Energy Storage. *J. Power Sources* **2015**, *297*, 23−32.

(5) Gorlin, Y.; Jaramillo, T. F. A Bifunctional Nonprecious Metal Catalyst for Oxygen Reduction and Water Oxidation. *J. Am. Chem. Soc.* **2010**, *132*, 13612−13614.

(6) Chen, G.; Bare, S. R.; Mallouk, T. E. Development of Supported Bifunctional Electrocatalysts for Unitized Regenerative Fuel Cells. *J. Electrochem. Soc.* **2002**, *149*, A1092−A1099.

(7) Katsounaros, I.; Cherevko, S.; Zeradjanin, A. R.; Mayrhofer, K. J. J. Oxygen Electrochemistry as A Cornerstone for Sustainable Energy Conversion. *Angew. Chem., Int. Ed.* **2014**, *53*, 102−121.

(8) Lu, Y.-C.; Gallant, B. M.; Kwabi, D. G.; Harding, J. R.; Mitchell, R. R.; Whittingham, M. S.; Shao-Horn, Y. Lithium-oxygen Batteries: Bridging Mechanistic Understanding and Battery Performance. *Energy Environ. Sci.* **2013**, *6*, 750−768.

(9) Girishkumar, G.; McCloskey, B.; Luntz, A. C.; Swanson, S.; Wilcke, W. Lithium Air Battery: Promise and Challenges. *J. Phys. Chem. Lett.* **2010**, *1*, 2193−2203.

(10) Kudo, A.; Miseki, Y. Heterogeneous Photocatalyst Materials for Water Splitting. *Chem. Soc. Rev.* **2009**, *38*, 253−278.

(11) Maeda, K.; Teramura, K.; Lu, D.; Takata, T.; Saito, N.; Inoue, Y.; Domen, K. Photocatalyst Releasing Hydrogen from Water. *Nature* **2006**, *440*, 295−295.

(12) Mao, S.; Wen, Z.; Huang, T.; Hou, Y.; Chen, J. High-Performance Bi-functional Electrocatalysts of 3D Crumpled Graphene-Cobalt Oxide Nanohybrids for Oxygen Reduction and Evolution Reactions. *Energy Environ. Sci.* **2014**, *7*, 609−616.

(13) Zhang, J.; Zhao, Z.; Xia, Z.; Dai, L. A Metal-free Bifunctional Electrocatalyst for Oxygen Reduction and Oxygen Evolution Reactions. *Nat. Nanotechnol.* **2015**, *10*, 444−452.

(14) Cheon, J. Y.; Kim, T.; Choi, Y.; Jeong, H. Y.; Kim, M. G.; Sa, Y. J.; Kim, J.; Lee, Z.; Yang, T.; Kwon, K.; Terasalo, O.; Park, G.; Adzic, R. R.; Joo, S. H. Ordered Mesoporous Porphyrinic Carbons with Very High Electrocatalytic Activity for the Oxygen Reduction Reaction. *Sci. Rep.* **2013**, *3*, 2715.

(15) Zhou, W.; Wu, X. J.; Cao, X.; Huang, X.; Tan, C.; Tian, J.; Liu, H.; Wang, J.; Zhang, H. Ni_3S_2 Nanorods/Ni Foam Composite Electrode with Low Overpotential for Electrocatalytic Oxygen Evolution. *Energy Environ. Sci.* **2013**, *6*, 2921−2924.

(16) Suntivich, J.; Gasteiger, H. A.; Yabuuchi, N.; Nakanishi, H.; Goodenough, J. B.; Shao-Horn, Y. Design Principles for Oxygen-Reduction Activity on Perovskite Oxide Catalysts for Fuel Cells and Metal-Air Batteries. *Nat. Chem.* **2011**, *3*, 546−550.

(17) Grimaud, A.; May, K. J.; Carlton, C. E.; Lee, Y. L.; Risch, M.; Hong, W. T.; Zhou, J.; Shao-Horn, Y. Double Perovskite as A Family of Highly Active Catalysts For Oxygen Evolution in Alkaline Solution. *Nat. Commun.* **2013**, *4*, 2439.

(18) Candelaria, S. L.; Shao, Y.; Zhou, W.; Li, X.; Xiao, J.; Zhang, J. G.; Wang, Y.; Liu, J.; Li, J.; Cao, G. Nanostructured Carbon for Energy Storage and Conversion. *Nano Energy* **2012**, *1*, 195−220.

(19) Bing, Y.; Liu, H.; Zhang, L.; Ghosh, D.; Zhang, J. Nanostructured Pt-Alloy Electrocatalysts for PEM Fuel Cell Oxygen Reduction Reaction. *Chem. Soc. Rev.* **2010**, *39*, 2184−2202.

(20) McCrory, C. C. L.; Jung, S.; Peters, J. C.; Jaramillo, T. F. Benchmarking Heterogeneous Electrocatalysts for the Oxygen Evolution Reaction. *J. Am. Chem. Soc.* **2013**, *135*, 16977−16987.

(21) Xu, J.; Aili, D.; Li, Q.; Christensen, E.; Jensen, J. O.; Zhang, W.; Hansen, M. K.; Liu, G.; Wang, X.; Bjerrum, N. J. Oxygen Evolution Catalysts on Supports with a 3-D Ordered Array Structure and Intrinsic Proton Conductivity for Proton Exchange Membrane Steam Electrolysis. *Energy Environ. Sci.* **2014**, *7*, 820−830.

(22) Zhao, A.; Masa, J.; Xia, W.; Maljusch, A.; Willinger, M. G.; Clavel, G.; Xie, K.; Schlögl, R.; Schuhmann, W.; Muhler, M. Spinel Mn-Co Oxide in N-Doped Carbon Nanotubes as a Bifunctional Electrocatalyst Synthesized by Oxidative Cutting. *J. Am. Chem. Soc.* **2014**, *136*, 7551−7554.

(23) Reier, T.; Oezaslan, M.; Strasser, P. Electrocatalytic Oxygen Evolution Reaction (OER) on Ru, Ir, and Pt Catalysts: A Comparative Study of Nanoparticles and Bulk Materials. *ACS Catal.* **2012**, *2*, 1765−1772.

(24) Mayrhofer, K. J. J.; Arenz, M. Fuel Cells: Log on for New Catalysts. *Nat. Chem.* **2009**, *1*, 518−519.

(25) Menezes, P. W.; Indra, A.; González-Flores, D.; Sahraie, N. R.; Zaharieva, I.; Schwarze, M.; Strasser, P.; Dau, H.; Driess, M. High-Performance Oxygen Redox Catalysis with Multifunctional Cobalt Oxide Nanochains: Morphology-Dependent Activity. *ACS Catal.* **2015**, *5*, 2017−2027.

(26) Hou, Y.; Wen, Z.; Cui, S.; Ci, S.; Mao, S.; Chen, J. H. An Advanced Nitrogen-Doped Graphene/Cobalt-Embedded Porous Carbon Polyhedron Hybrid for Efficient Catalysis of Oxygen Reduction and Water Splitting. *Adv. Funct. Mater.* **2015**, *25*, 872−882.

(27) Niu, W.; Li, L.; Liu, X.; Wang, N.; Liu, J.; Zhou, W.; Tang, Z.; Chen, S. Mesoporous N-Doped Carbons Prepared with Thermally Removable Nanoparticle Templates: An Efficient Electrocatalyst for Oxygen Reduction Reaction. *J. Am. Chem. Soc.* **2015**, *137*, 5555−5562.

(28) Jaouen, F.; Proietti, E.; Lefèvre, M.; Chenitz, R.; Dodelet, J.-P.; Wu, G.; Chung, H. T.; Johnston, C. M.; Zelenay, P. Recent Advances in Non-Precious Metal Catalysis for Oxygen-Reduction Reaction in Polymer Electrolyte Fuel Cells. *Energy Environ. Sci.* **2011**, *4*, 114−130.

(29) Xiang, Z.; Xue, Y.; Cao, D.; Huang, L.; Chen, J.-F.; Dai, L. Highly Efficient Electrocatalysts for Oxygen Reduction Based on 2D Covalent Organic Polymers Complexed with Non-Precious Metals. *Angew. Chem., Int. Ed.* **2014**, *53*, 2433−2437.

(30) Liang, H.-W.; Wei, W.; Wu, Z.-S.; Feng, X.; Müllen, K. Mesoporous Metal-Nitrogen-Doped Carbon Electrocatalysts for

DOI: 10.1021/acsami.5b06708
ACS Appl. Mater. Interfaces 2015, 7, 21511−21520

Highly Efficient Oxygen Reduction Reaction. *J. Am. Chem. Soc.* **2013**, *135*, 16002−16005.
(31) Mao, S.; Wen, Z.; Huang, T.; Hou, Y.; Chen, J. High-Performance Bi-functional Electrocatalysts of 3D Crumpled Graphene-Cobalt Oxide Nanohybrids for Oxygen Reduction and Evolution Reactions. *Energy Environ. Sci.* **2014**, *7*, 609−616.
(32) Xiao, M.; Zhu, J.; Feng, L.; Liu, C.; Xing, W. Meso/Macroporous Nitrogen-Doped Carbon Architectures with Iron Carbide Encapsulated in Graphitic Layers as An Efficient and Robust Catalyst for the Oxygen Reduction Reaction in Both Acidic and Alkaline Solutions. *Adv. Mater.* **2015**, *27*, 2521−2527.
(33) Wen, Z.; Ci, S.; Hou, Y.; Chen, J. Facile One-Pot, One-Step Synthesis of A Carbon Nanoarchitecture for An Advanced Multi-functonal Electrocatalyst. *Angew. Chem., Int. Ed.* **2014**, *53*, 6496−6500.
(34) Deng, D.; Yu, L.; Chen, X.; Wang, G.; Jin, L.; Pan, X.; Deng, J.; Sun, G.; Bao, X. Iron Encapsulated within Pod-like Carbon Nanotubes for Oxygen Reduction Reaction. *Angew. Chem., Int. Ed.* **2013**, *52*, 371−375.
(35) Chen, W.; Fan, Z.; Pan, X.; Bao, X. Effect of Confinement in Carbon Nanotubes on the Activity of Fischer−Tropsch Iron Catalyst. *J. Am. Chem. Soc.* **2008**, *130*, 9414−9419.
(36) Hu, Y.; Jensen, J. O.; Zhang, W.; Cleemann, L. N.; Xing, W.; Bjerrum, N. J.; Li, Q. Hollow Spheres of Iron Carbide Nanoparticles Encased in Graphitic Layers as Oxygen Reduction Catalysts. *Angew. Chem., Int. Ed.* **2014**, *53*, 3675−3679.
(37) Ambrosi, A.; Chua, C. K.; Bonanni, A.; Pumera, M. Electrochemistry of Graphene and Related Materials. *Chem. Rev.* **2014**, *114*, 7150−7188.
(38) Jin, J.; Pan, F.; Jiang, L.; Fu, X.; Liang, A.; Wei, Z.; Zhang, J.; Sun, G. Catalyst-Free Synthesis of Crumpled Boron and Nitrogen Co-Doped Graphite Layers with Tunable Bond Structure for Oxygen Reduction Reaction. *ACS Nano* **2014**, *8*, 3313−3321.
(39) Cui, W.; Cheng, N.; Liu, Q.; Ge, C.; Asiri, A. M.; Sun, X. Mo_2C Nanoparticles Decorated Graphitic Carbon Sheets: Biopolymer-Derived Solid-State Synthesis and Application as An Efficient Electrocatalyst for Hydrogen Generation. *ACS Catal.* **2014**, *4*, 2658−2661.
(40) Hao, L.; Zhang, S.; Liu, R.; Ning, J.; Zhang, G.; Zhi, L. Bottom-Up Construction of Triazine-Based Frameworks as Metal-Free Electrocatalysts for Oxygen Reduction Reaction. *Adv. Mater.* **2015**, *27*, 3190−3195.
(41) Paulus, U. A.; Schmidt, T. J.; Gasteiger, H. A.; Behm, R. J. Oxygen Reduction on A High-Surface Area Pt/Vulcan Carbon Catalyst: A Thin-Film Rotating Ring-Disk Electrode Study. *J. Electroanal. Chem.* **2001**, *495*, 134−145.
(42) Zhang, Y.; Liu, J.; Wu, G.; Chen, W. Porous Graphitic Carbon Nitride Synthesized via Direct Polymerization of Urea for Efficient Sunlight-Driven Photocatalytic Hydrogen Production. *Nanoscale* **2012**, *4*, 5300−5303.
(43) Li, X.; Kurasch, S.; Kaiser, U.; Antonietti, M. Synthesis of Monolayer-Patched Graphene from Glucose. *Angew. Chem., Int. Ed.* **2012**, *51*, 9689−9692.
(44) Li, X.; Antonietti, M. Polycondensation of Boron- and Nitrogen-Codoped Holey Graphene Monoliths from Molecules: Carbocatalysts for Selective Oxidation. *Angew. Chem., Int. Ed.* **2013**, *52*, 4572−4576.
(45) Geng, D. S.; Chen, Y.; Chen, Y. G.; Li, Y. L.; Li, R. Y.; Sun, X. L.; Ye, S. Y.; Knights, S. High Oxygen-Reduction Activity and Durability of Nitrogen-Doped Graphene. *Energy Environ. Sci.* **2011**, *4*, 760−764.
(46) Qu, L. T.; Liu, Y.; Baek, J. B.; Dai, L. M. Nitrogen-Doped Graphene as Efficient Metal-Free Electrocatalyst for Oxygen Reduction in Fuel Cells. *ACS Nano* **2010**, *4*, 1321−1326.
(47) Maldonado-Hodar, F. J.; Moreno-Castilla, C.; Rivera-Utrilla, J.; Hanzawa, Y.; Yamada, Y. Catalytic Graphitization of Carbon Aerogels by Transition Metals. *Langmuir* **2000**, *16*, 4367−4373.
(48) Su, Y.; Jiang, H.; Zhu, Y.; Yang, X.; Shen, J.; Zou, W.; Chen, J.; Li, C. Enriched Graphitic N-Doped Carbon-Supported Fe_3O_4 Nanoparticles as Efficient Electrocatalysts for Oxygen Reduction Reaction. *J. Mater. Chem. A* **2014**, *2*, 7281−7287.
(49) Jeon, I.-Y.; Zhang, S.; Zhang, L.; Choi, H.-J.; Seo, J.-M.; Xia, Z.; Dai, L.; Baek, J.-B. Edge-Selectively Sulfurized Graphene Nanoplatelets as Efficient Metal-Free Electrocatalysts for Oxygen Reduction Reaction: the Electron Spin Effect. *Adv. Mater.* **2013**, *25*, 6138−6145.
(50) Jiang, H.; Zhu, Y.; Feng, Q.; Su, Y.; Yang, X.; Li, C. Nitrogen and Phosphorus Dual-Doped Hierarchical Porous Carbon Foams as Efficient Metal-Free Electrocatalysts for Oxygen Reduction Reactions. *Chem. - Eur. J.* **2014**, *20*, 3106−3112.
(51) Jiang, H.; Zhu, Y.; Su, Y.; Yao, Y.; Liu, Y.; Yang, X.; Li, C. Highly Dual-Doped Multilayer Nanoporous Graphene: Efficient Metal-Free Electrocatalysts for the Hydrogen Evolution Reaction. *J. Mater. Chem. A* **2015**, *3*, 12642−12645.
(52) Lin, Z.; Waller, G.; Liu, Y.; Liu, M.; Wong, C. Facile Synthesis of Nitrogen-Doped Graphene via Pyrolysis of Graphene Oxide and Urea, and its Electrocatalytic Activity Toward the Oxygen-Reduction Reaction. *Adv. Energy Mater.* **2012**, *2*, 884−888.
(53) Lin, L.; Zhu, Q.; Xu, A. W. Noble-Metal-Free Fe-N/C Catalyst for Highly Efficient Oxygen Reduction Reaction under Both Alkaline and Acidic Conditions. *J. Am. Chem. Soc.* **2014**, *136*, 11027−11033.
(54) Li, Y.; Zhou, W.; Wang, H.; Xie, L.; Liang, Y.; Wei, F.; Idrobo, J. C.; Pennycook, S. J.; Dai, H. An Oxygen Reduction Electrocatalyst based on Carbon Nanotube-Graphene Complexes. *Nat. Nanotechnol.* **2012**, *7*, 394−400.
(55) Wu, G.; Chen, Z. W.; Artyushkova, K.; Garzon, F. H.; Zelenay, P. Polyaniline-Derived Non-Precious Catalyst for the Polymer Electrolyte Fuel Cell Cathode. *ECS Trans.* **2008**, *16*, 159−164.
(56) Peng, H.; Mo, Z.; Liao, S.; Liang, H.; Yang, L.; Luo, F.; Song, H.; Zhong, Y.; Zhang, B. High Performance Fe-and N-doped Carbon Catalyst with Graphene Structure for Oxygen Reduction. *Sci. Rep.* **2013**, *3*, 1765.
(57) Wu, G.; More, K. L.; Johnston, C. M.; Zelenay, P. High-Performance Electrocatalysts for Oxygen Reduction Derived from Polyaniline, Iron, and Cobalt. *Science* **2011**, *332*, 443−447.
(58) Ferrandon, M.; Kropf, A. J.; Myers, D. J.; Artyushkova, K.; Kramm, U.; Bogdanoff, P.; Wu, G.; Johnston, C. M.; Zelenay, P. Multitechnique Characterization of a Polyaniline-Iron-Carbon Oxygen Reduction Catalyst. *J. Phys. Chem. C* **2012**, *116*, 16001−16013.
(59) Lee, J.-S.; Kim, S. T.; Cao, R.; Choi, N.-S.; Liu, M.; Lee, K. T.; Cho, J. Metal-Air Batteries with High Energy Density: Li-Air versus Zn-Air. *Adv. Energy Mater.* **2011**, *1*, 34−50.
(60) Bruce, P. G.; Freunberger, S. A.; Hardwick, L. J.; Tarascon, J.-M. Li-O_2 and Li-S Batteries with High Energy Storage. *Nat. Mater.* **2012**, *11*, 19−29.
(61) Matsumoto, Y.; Sato, E. Electrocatalytic Properties of Transition-Metal Oxides for Oxygen Evolution Reaction. *Mater. Chem. Phys.* **1986**, *14*, 397−426.
(62) Ma, T. Y.; Dai, S.; Jaroniec, M.; Qiao, S. Z. Graphitic Carbon Nitride Nanosheet-Carbon Nanotube Three-Dimensional Porous Composites as High-Performance Oxygen Evolution Electrocatalysts. *Angew. Chem., Int. Ed.* **2014**, *53*, 7281−7285.
(63) Tian, J.; Liu, Q.; Asiri, A. M.; Alamry, K. A.; Sun, X. Ultrathin Graphitic C_3N_4 Nanosheets/Graphene Composites: Efficient Organic Electrocatalyst for Oxygen Evolution Reaction. *ChemSusChem* **2014**, *7*, 2125−2130.
(64) Zou, X.; Huang, X.; Goswami, A.; Silva, R.; Sathe, B. R.; Mikmekova, E.; Asefa, T. Cobalt-Embedded Nitrogen-Rich Carbon Nanotubes Efficiently Catalyze Hydrogen Evolution Reaction at All pH Values. *Angew. Chem., Int. Ed.* **2014**, *53*, 4372−4376.
(65) Li, M.; Zhang, L.; Xu, Q.; Niu, J.; Xia, Z. N-doped Graphene as Catalysts for Oxygen Reduction and Oxygen Evolution Reactions: Theoretical Considerations. *J. Catal.* **2014**, *314*, 66−72.
(66) Kim, H.; Lee, K.; Woo, S. I.; Jung, Y. On the Mechanism of Enhanced Oxygen Reduction Reaction in Nitrogen-Doped Graphene Nanoribbons. *Phys. Chem. Chem. Phys.* **2011**, *13*, 17505−17510.
(67) Wiesener, K. N_4-Chelates as Electrocatalyst for Cathodic Oxygen Reduction. *Electrochim. Acta* **1986**, *31*, 1073−1078.
(68) Strickland, K.; Miner, E.; Jia, Q.; Tylus, U.; Ramaswamy, N.; Liang, W.; Sougrati, M.-T.; Jaouen, F.; Mukerjee, S. Highly Active Oxygen Reduction Non-Platinum Group Metal Electrocatalyst

DOI: 10.1021/acsami.5b06708
ACS Appl. Mater. Interfaces 2015, 7, 21511−21520

Without Direct Metal-Nitrogen Coordination. *Nat. Commun.* **2015**, *6*, 7343.
(69) Zhao, Y.; Kamiya, K.; Hashimoto, K.; Nakanishi, S. Efficient Bifunctional Fe/C/N Electrocatalysts for Oxygen Reduction and Evolution Reaction. *J. Phys. Chem. C* **2015**, *119*, 2583−2588.
(70) Li, J.; Li, S.; Tang, Y.; Han, M.; Dai, Z.; Bao, J.; Lan, Y. Nitrogen-Doped Fe/Fe_3C@ Graphitic Layer/Carbon Nanotube Hybrids Derived from MOFs: Efficient Bifunctional Electrocatalysts for ORR and OER. *Chem. Commun.* **2015**, *51*, 2710−2713.

DOI: 10.1021/acsami.5b06708
ACS Appl. Mater. Interfaces 2015, 7, 21511−21520